High Power Laser Science and Engineering, (2024), Vol. 12, e11, 8 pages.
doi:10.1017/hpl.2023.92

HIGH POWER LASER SCIENCE AND ENGINEERING

RESEARCH ARTICLE

Prospect of ultrahigh-resolution fast neutron absorption spectroscopy based on a laser plasma electron accelerator

Wen-Zhao Wang[1,2], Jie Feng[1,2], Xiao-Peng Zhang[3], Yao-Jun Li[1,2], Wei-Jun Zhou[1,2], Wen-Chao Yan[1,2], Guo-Qiang Zhang[4], Chang-Bo Fu[5], and Li-Ming Chen[1,2]

[1] *Key Laboratory of Laser Plasma (MoE), School of Physics and Astronomy, Shanghai Jiao Tong University, Shanghai, China*

[2] *IFSA Collaborative Innovation Center, Shanghai Jiao Tong University, Shanghai, China*

[3] *Institute of High Energy Physics, Chinese Academy of Sciences, Beijing, China*

[4] *Shanghai Advanced Research Institute, Chinese Academy of Sciences, Shanghai, China*

[5] *Key Laboratory of Nuclear Physics and Ion-beam Application (MoE), Institute of Modern Physics, Fudan University, Shanghai, China*

(Received 21 June 2023; revised 25 October 2023; accepted 23 November 2023)

Abstract

Fast neutron absorption spectroscopy is widely used in the study of nuclear structure and element analysis. However, due to the traditional neutron source pulse duration being of the order of nanoseconds, it is difficult to obtain a high-resolution absorption spectrum. Thus, we present a method of ultrahigh energy-resolution absorption spectroscopy via a high repetition rate, picosecond duration pulsed neutron source driven by a terawatt laser. The technology of single neutron count is used, which results in easily distinguishing the width of approximately 20 keV at 2 MeV and an asymmetric shape of the neutron absorption peak. The absorption spectroscopy based on a laser neutron source has one order of magnitude higher energy-resolution power than the state-of-the-art traditional neutron sources, which could be of benefit for precisely measuring nuclear structure data.

Keywords: fast neutron absorption spectroscopy; laser plasma accelerator; photo-nuclear neutrons; single neutron count

1. Introduction

Fast neutron absorption spectroscopy (FNAS) based upon traditional accelerators or reactors has applications in many regions, including the non-destructive testing of goods[1–3], the measurement of nucleus fine structures[4,5], the study of material characteristics[6,7], etc. The energy resolution of FNAS is mainly limited by the duration of the neutron source, and the traditional fast neutron source is usually longer than 1 nanosecond (ns)[8–10]. So far, the energy resolution of the state-of-the-art traditional source is approximately 100 keV at 3 MeV, which makes it impossible for this source to accurately measure the width or shape of resonance absorption peaks of nuclei, for example, ^{16}O $\sim$ 5 keV full width at half maximum (FWHM) at 1.65 MeV[11,12].

The laser plasma wakefield accelerator (LWFA) has attracted significant interest in the past decades[13–15], due to the extremely high acceleration gradient and beam current[16,17], thus enabling GeV electron accelerators at the tabletop level, as well as driving secondary radiation/particle sources with ultrahigh brightness/flux[11,18]. LWFAs have achieved many successes in recent years, including record beam energy of up to 8 GeV in cm length[19], beam duration down to femtoseconds (fs), driven X-ray free-electron lasers[20–22], etc. Moreover, the LWFA fs duration electron beam can drive ultra-fast Bremsstrahlung γ-ray photons in a thin metal target, and further induce photo-nuclear reactions to realize a tens of picoseconds (ps) pulse duration fast neutron source, which has great potential to improve the energy resolution of FNAS[6] two orders of magnitude higher than traditional fast neutron sources[11,12].

However, in experiments, it is difficult for the laser-driven ps duration pulsed fast neutron source to realize a fine absorption spectrum in a single shot, due to the low yield[23–26] and, in particular, the slow temporal response of the neutron time-of-flight (nTOF) detector[27]. In recent

Correspondence to: Jie Feng and Li-Ming Chen, Key Laboratory of Laser Plasma (MoE), School of Physics and Astronomy, Shanghai Jiao Tong University, Shanghai 200240, China. Email: fengjie93@sjtu.edu.cn (J. Feng); lmchen@sjtu.edu.cn (L.-M. Chen)

years, the technology of using a kilohertz (kHz) laser facility to drive high repetition rate electron beams has become mature[28–30] and the electron energy could be up to 15 MeV, which is suitable to drive photo-nuclear neutrons[30]. Although a kHz laser facility can be used to drive electron beams with suitable energy, the beam charge is only several picocoulombs, which is limited by the laser energy of several millijoules (mJ)[29]. The yield of the neutron driven by this electron beam would be too low for the application of FNAS. Notably, Papp *et al.*[31] have theoretically realized a hundreds of pC electron beam via a 100 mJ repetition rate laser, which could greatly enhance the neutron yield. In addition, the temporal resolution of the nTOF method is about tens of ns due to the rising edge and afterglow of the scintillator detector, with which it is hard to distinguish two fast neutron pulses with a small difference in arrival time. Thus, it is difficult to acquire a high-resolution neutron energy spectrum from the single-shot nTOF[27].

In order to solve the above two key problems simultaneously, firstly, we proposed a method to enhance the LWFA electron beam charge to several nanocoulombs (nC) by utilizing a 100-mJ 100-hertz (hHz) laser system. In general, a faster response or longer nTOF detection distance means higher energy resolution. Secondly, we proposed a method named single-neutron-count (SNC) TOF to reduce the influence of the detector response speed and detection distance, as separated single neutron signals are easy to diagnose. Finally, we showed the potential applications of ultrahigh FNAS based upon an hHz LWFA neutron source.

2. Design of an efficient laser plasma electron accelerator

The laser plasma accelerator is based on a commercial hHz laser system, which has been equipped in many laboratories, for example, it can deliver laser pulses with energy of 50 mJ, pulse duration of 30 fs in FWHM and repetition rate of 100 Hz. The laser pulses can be focused into the gas jet with an $f/3$ off-axis paraboloid mirror to a spot size $w_0 = 2.5$ μm (1.2 times the diffraction limit) containing 80% of the total energy, giving a confocal parameter of $2z_R \sim 50$ μm (z_R is Rayleigh length) and a peak intensity of 8.5×10^{18} W/cm^2 (peak normalized vector potential $a_0 = 2$). The dense gas jet is generated by feeding high-pressure nitrogen gas through a solenoid valve to a Mach ~3 supersonic 'De Laval' nozzle with a 100 μm diameter throat and a 300 μm exit diameter[32]. The out-flow gas density profile is near-Gaussian distribution with approximately 120 μm in FWHM, according to the computational fluid dynamics simulation using ANSYS Fluent software. The peak nitrogen density can be adjusted in the range of $n_N = 0.5 \times 10^{19} - 5 \times 10^{19}$ cm^{-3} by controlling the gas backing pressure. After the LWFA process, the electron beam passes through the Kapton window, and then it is deflected by a magnet and bombards on the Lanex emitting fluorescence, which is collected by a charge-coupled device (CCD) for acquiring a beam energy spectrum[33], as shown in Figure 1. In experiments, some parameters, for example, the laser focal position, gas density, and laser pulse second order dispersion, can be adjusted to optimize the electron beam quality.

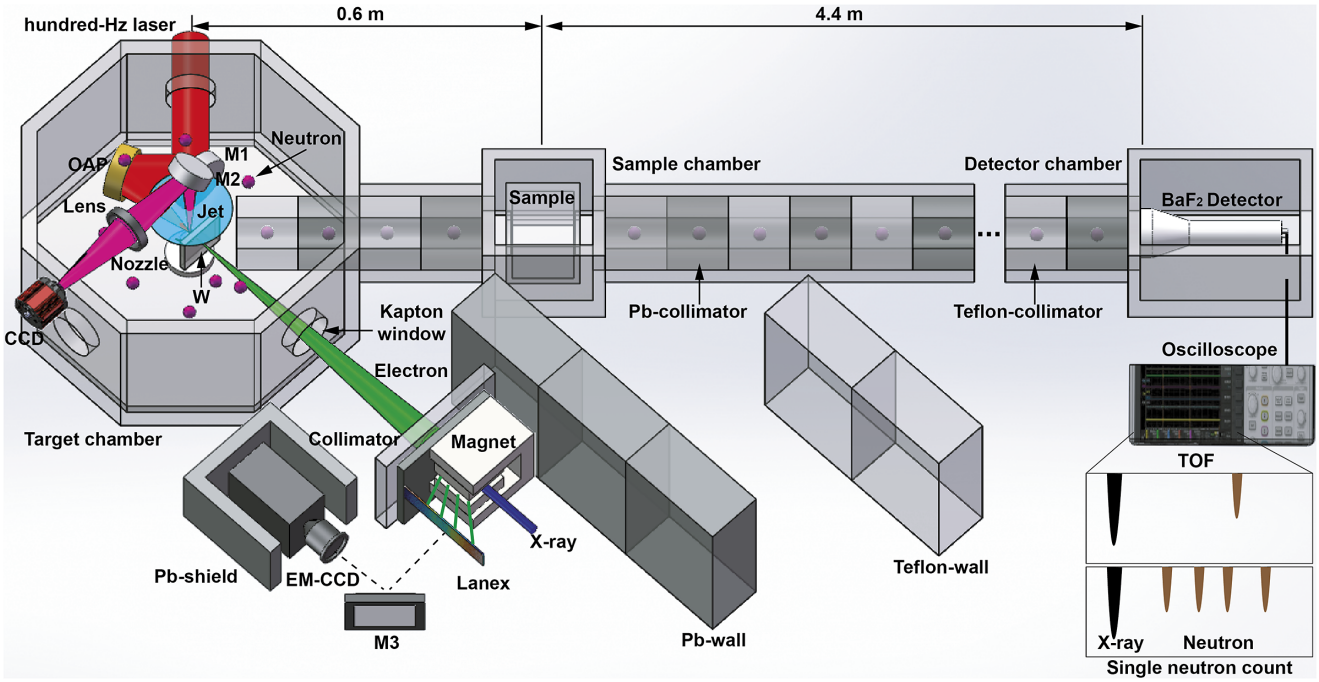

Figure 1. Design of the experimental setup for the generation of an ultra-short pulsed neutron source and the fast neutron absorption spectroscopy.

https://doi.org/10.1017/hpl.2023.92 Published online by Cambridge University Press

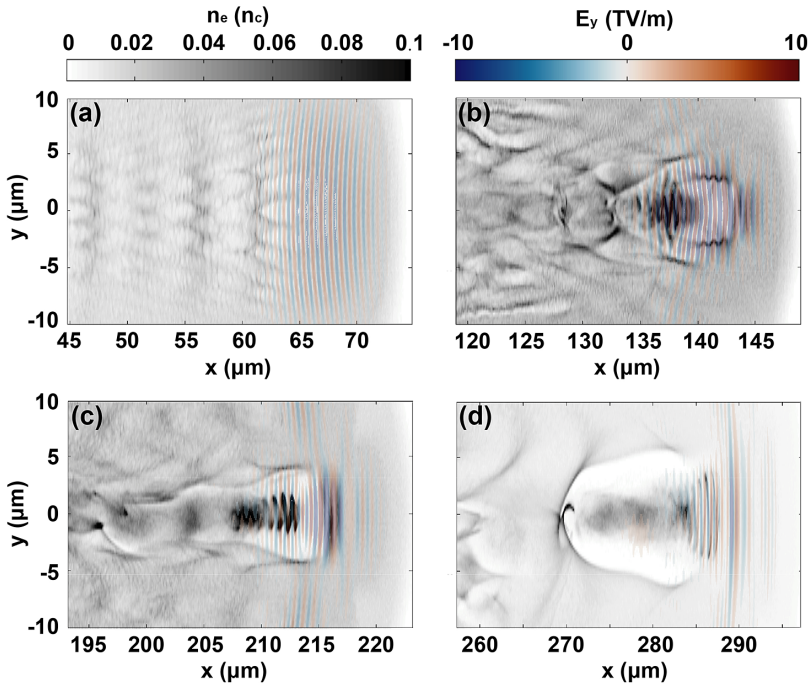

Figure 2. Three-dimensional particle-in-cell simulations of laser plasma acceleration. (a)–(d) represent four different times at 0.25, 0.5, 0.75 and 1 ps, respectively. The nitrogen atom density is 1×10^{19} cm^{-3} and the laser $a_0 = 2$.

In order to exhibit the characteristics of the electron beam accelerated from the above system, we have carried out 3D particle-in-cell simulations using EPOCH code[34]. The simulation window size is set to 40 μm × 40 μm × 40 μm with 1200 × 300 × 300 cells in the *x*-, *y*- and *z*-directions, respectively. The simulation window propagates along the *x*-direction at the speed of light. One macro-particle per cell is used as the nitrogen atoms. The ionization process is modeled with ADK rates[35]. The longitudinal profile of nitrogen gas has a Gaussian distribution with 120 μm in FWHM. A laser pulse with p-polarization propagates along the *x*-axis, and it is focused at the center of the nitrogen gas profile. Both the focal spot and pulse envelope have Gaussian profiles, $w_0 = 2.5$ μm and the pulse duration is 30 fs. The laser intensity is set to 8.5×10^{18} W/cm^2.

To acquire a large charge and high conversion-efficiency electron beam, we scanned the gas density. In order to meet the matching criteria for maintaining laser intensity and overcoming quick defocus[36], that is, $w_0 \approx R$, where $R = 2c\sqrt{a_0}/\sqrt{4\pi n_e e^2/m_e}$ is the plasma bubble radius, usually requires a higher plasma density for matching the small focal spot. When considering a higher plasma density of 7×10^{19} cm^{-3}, the matched plasma bubble radius is approximately 2 μm, as a result of which the laser peak intensity can be further increased to $a_0 \sim 2.5$ due to self-focusing, as shown in Figure 2(b). The intense laser pulse will also induce the nonlinear evolution of plasma bubbles, which results in the combination of plasma bubbles and trapping a large number of electrons[16], as shown in Figure 2(c). Then, when the laser pulse propagates at the density down-ramp of the nitrogen gas jet, the accelerated intense electron beam drives plasma wakefield acceleration due to the fact that the tightly focused laser pulse quickly defocuses in low-density plasma, as shown in Figure 2(d). The self-generated electro-magnetic fields in the plasma bubbles would also restrain the electron beam[37], resulting in a micro-sized electron beam (∼4 μm in FWHM). Meanwhile, the electron beam has the advantages of ultra-short duration (∼30 fs in FWHM) and ultra-dense density ($\sim 1 \times 10^{20}$ cm^{-3}), which are unattainable for traditional radio-frequency accelerators.

Here, we have scanned the nitrogen density, and the results are shown in Figure 3. On increasing the density, the accelerated electron beam charge is quickly increased to approximately 2.8 nC ($E_k > 1$ MeV), as shown in Figure 3(a). Moreover, the maximum energy of the electron beam increases with the density, and can reach approximately 25 MeV, as shown in Figure 3(b). However, both the beam charge and the maximum energy decrease at densities above 1.5×10^{19} cm^{-3} due to the rapid dissipation of the driving laser in high-density plasma. Finally, we choose $n_N = 1 \times 10^{19}$ cm^{-3}, $a_0 = 2$ as the optimal conditions, and the electron parameters include charge 2.5 nC, source size 4 μm, maximum energy 25 MeV and divergence angle 5°. Significantly, most of the electrons have energy locating in the range of 7–20 MeV, which is beneficial for driving nuclear giant dipole resonance to produce fast neutrons via (γ, n) reactions.

https://doi.org/10.1017/hpl.2023.92 Published online by Cambridge University Press

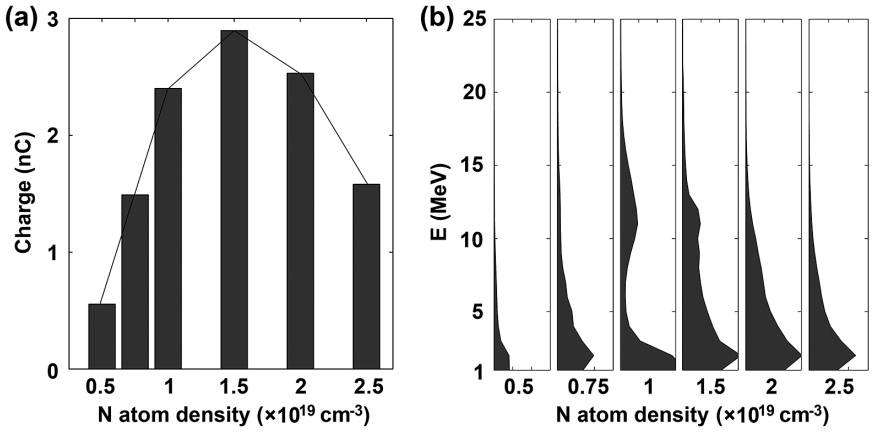

Figure 3. Simulation results of the electron beam. (a) Variation of electron beam charge ($E_k > 1$ MeV) with the nitrogen atom density. (b) Electron energy spectra for different nitrogen atom densities.

3. Generation of the ultra-short pulsed fast neutron source

To generate a fast neutron source, we have utilized the optimal electron beam to bombard a thin metal target for inducing photo-nuclear reactions[38]. Here, we carried out Monte Carlo simulation with Geant4 code. In the simulation setup, the metal target is a piece of tantalum (Ta) sheet with the thickness of 500 μm, which is set at 500 μm away from the electron beam source. The parameters of the electron beam, including the source size, distribution, energy spectrum and transversal momentum distribution, are imported into the input text of the Geant4 code, and 6.25×10^8 electrons are used in this Monte Carlo simulation.

The simulation results of the Bremsstrahlung source are shown in Figure 4. According to the γ-ray spectrum, most photons have energy below 15 MeV, and thus the neutrons would be mainly contributed by the $^{181}\mathrm{Ta}(\gamma,\mathrm{n})^{180}\mathrm{Ta}$ reaction, and a small number of neutrons are contributed by the $^{181}\mathrm{Ta}(\gamma,2\mathrm{n})^{179}\mathrm{Ta}$ reaction. In addition, the γ-ray source size is large (~50 μm in FWHM), due to the divergence of the electron beam in the Ta sheet.

The simulation results of the photo-nuclear neutron are shown in Figure 5. The fast neutron source has near-Gaussian transversal distribution and its source size is approximately 250 μm in FWHM, which is larger than that of the γ-ray source due to the neutrons' near-uniform emission distribution, as shown in Figures 5(a) and 5(b). The energy spectrum of the neutron source is shown in Figure 5(c). The neutron energy is mainly in the range from 40 keV to 4 MeV, and the peak energy is approximately 700 keV. The neutron yield considering the electron beam charge of 2.5 nC is shown in Figure 5(d). The yield increases rapidly with the target thickness, and the yield could be up to 7×10^5 for the 500 μm thickness. We estimated the neutron pulse duration according to the neutron energy spectra and target thickness, that is, $\Delta t = 73 \cdot d\,[\mathrm{mm}] \cdot \left(\frac{1}{\sqrt{E_{\mathrm{nl}}[\mathrm{MeV}]}} - \frac{1}{\sqrt{E_{\mathrm{nh}}[\mathrm{MeV}]}}\right)$[39], where d is the propagation distance (or the converter thickness) and E_{nl} and E_{nh} represent the low and high neutron kinetic energy in this pulse, respectively. The pulse duration is linearly proportional with the target thickness, and could be less than 50 ps for the 500 μm thickness, as shown in Figure 5(d).

4. Design of ultrahigh energy-resolution neutron absorption spectroscopy

The FNAS energy resolution is limited by three factors, the neutron pulse duration, detection distance and detector temporal resolution. At present, the doped BaF_2 crystal scintillator can realize an approximately 30 ps fluorescence process and an approximately hundreds of ps quenching process[40]. It has sufficiently high temporal resolution to be used to diagnose the arrival time of a neutron. For the effects of detection distance, the farther the distance, the higher the energy resolution[12]. Here, it is limited by the single-shot yield of the laser neutron source, and we set the detection distance to 5 m. For the case of 1.5 MeV neutron energy and 1 ns pulse duration, $\frac{\Delta E}{E} = 52.8$ keV @ 5 m, 1 ns, and even if the detection distance of 20 m corresponds to an energy resolution of 13.2 keV @ 1.5 MeV, 1 ns[12], it is still difficult for the state-of-the-art traditional fast neutron source to acquire the FNAS, which can exhibit the fine structure of some resonance absorption peaks[11,12].

In order to further decrease the influence of scintillator fluorescence tailing on the energy resolution of FNAS, we proposed a method named SNC absorption spectroscopy, for which the setup is shown in Figure 1. The generated photo-nuclear neutron source has near-uniform distribution in the entire 4π solid angle. Here, we choose the 45° direction and use a long vacuum tube composed of Teflon and lead collimators with a hole diameter 5 cm to transport the fast neutrons. The sample and the BaF_2 detector are placed

https://doi.org/10.1017/hpl.2023.92 Published online by Cambridge University Press

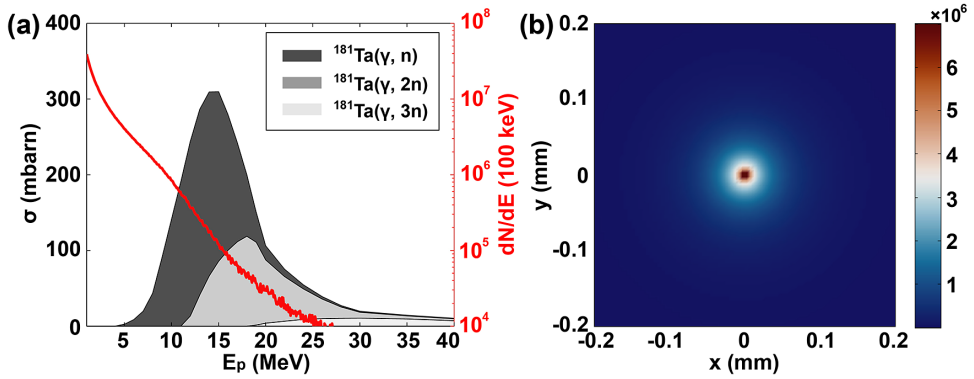

Figure 4. Simulation results of the Bremsstrahlung source driven by the laser plasma electron accelerator. (a) γ-ray spectrum (red line) photo-nuclear reactions of ^{181}Ta(γ, n), ^{181}Ta(γ, 2n) and ^{181}Ta(γ, 3n). (b) γ-ray source transversal distribution, which is detected on the plane of the rear surface of the Ta converter.

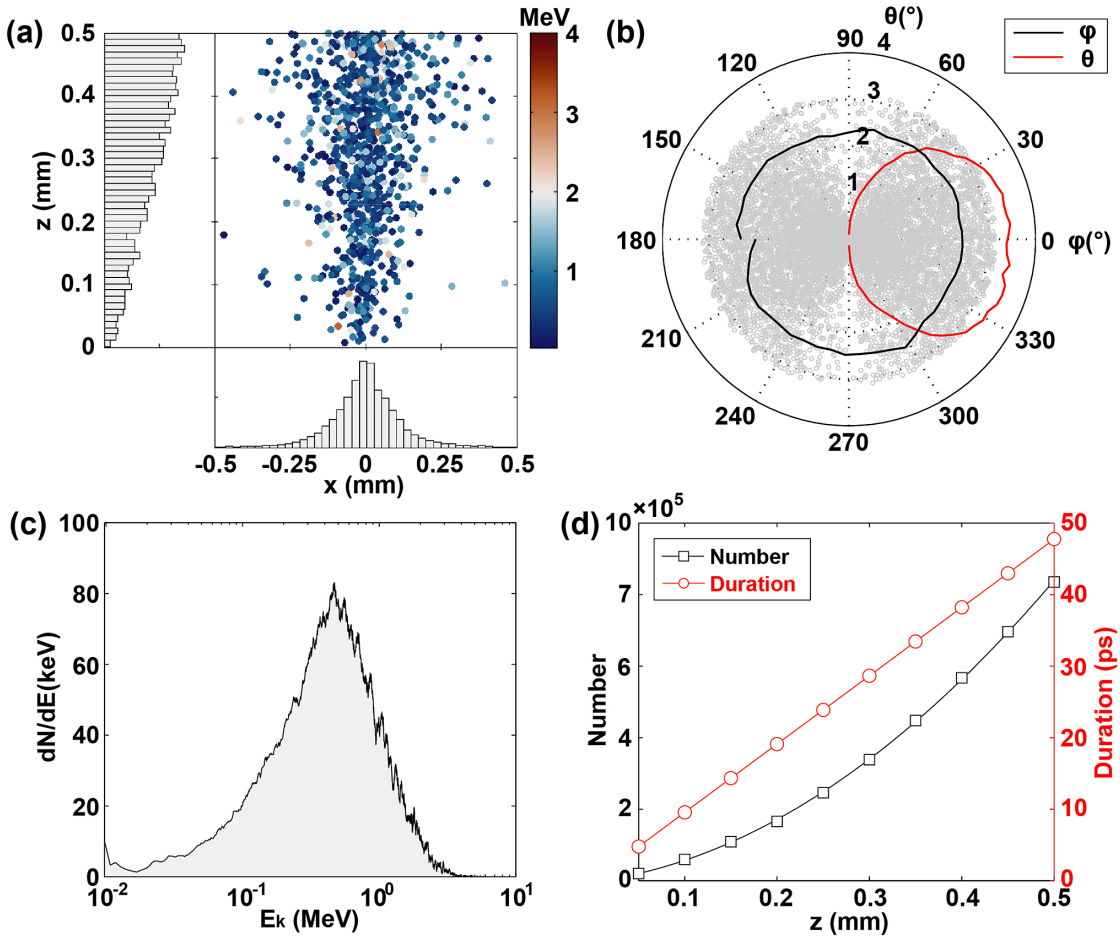

Figure 5. Simulation results of the neutron source driven by the laser plasma electron accelerator. (a) Neutron spatial distribution. (b) Neutron angular distribution. (c) Neutron energy spectrum. (d) Neutron yield and pulse duration.

0.6 and 5 m away from the neutron source point, respectively. By considering the neutron yield of 7×10^5 neutrons/shot and the response efficiency of the BaF_2 detector of approximately 20% for fast neutrons, approximately four neutrons can be recorded on the oscilloscope for one laser shooting. The signal is several separated peaks or only one peak, and we can calculate their energy according to the time-of-flight signal on the oscilloscope. Finally, we accumulate enough shots to acquire the neutron energy spectrum or absorption spectrum.

As the results show in Figure 6, we present the potential of this kind of FNAS. The sample is composed of two

https://doi.org/10.1017/hpl.2023.92 Published online by Cambridge University Press

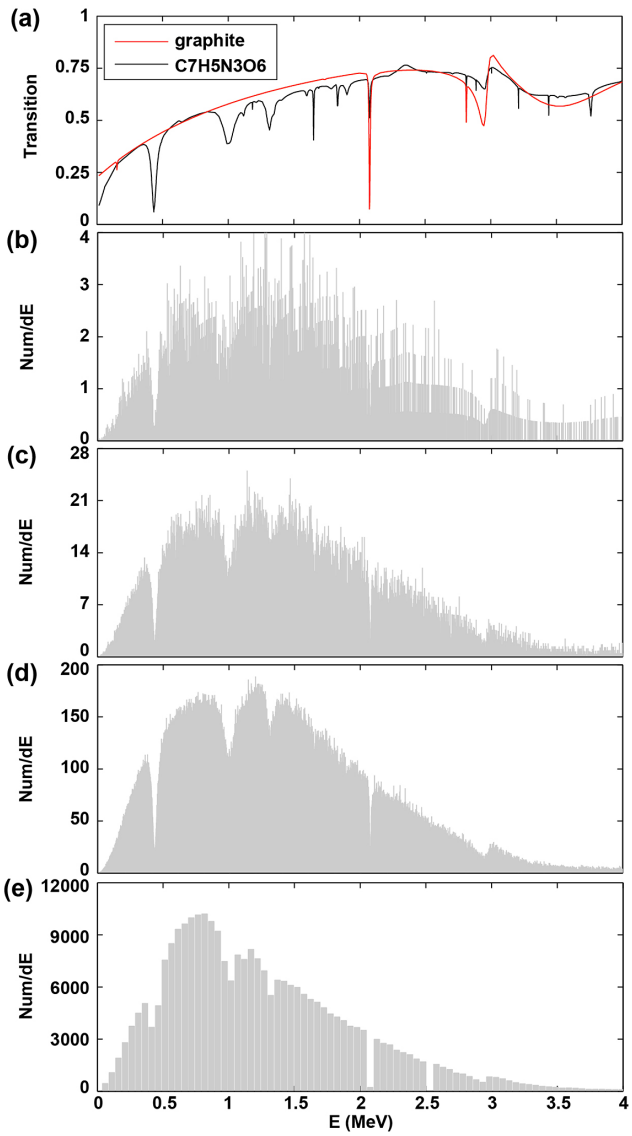

Figure 6. Single-neutron-count fast neutron absorption spectroscopy. (a) Transmissivities for two materials, that is, graphite and TNT. (b)–(d) Simulated neutron absorption spectrum for the pulse duration of 36 ps, where the total neutron counts are 10^4 (b), 10^5 (c) and 10^6 (d), respectively. (e) Absorption spectrum for the pulse duration of 1 ns, where the total count is 10^6.

materials, namely graphite and C7H5N3O6 (TNT), and the neutron transmittances of the two materials are shown in Figure 6(a). In the simulation, the neutron beam with the energy spectrum of Figure 5(c) passes through the sample; then one transmitted neutron is randomly selected via MATLAB code to be recorded and the recorded energy has corresponding uncertainty, which is shown in Ref. [12] (Figure 5(b)); finally, we repeat the selection process to accumulate enough transmitted neutrons to acquire a fine absorption spectrum, whose energy resolution is determined by the calculated result in Ref. [12]; the repetitive process is the same to accumulate laser shots. The absorption spectra are shown in Figures 6(b)–6(d). For the case of accumulating 10^4 neutrons, the absorption peak at 433 keV can be distinguished clearly, but the absorption peak width of approximately 60 keV in FWHM is larger than that of 40 keV from the theoretical data[41], as shown in Figure 6(b). When the neutron number is increased to 10^5, the FWHM at 433 keV could be close to the theoretical value of approximately 40 keV. Moreover, we continue to accumulate the neutron number to 10^6 (which means 2.5×10^5 shots or almost 4 h in our experimental case), the absorption peak at 2080 keV with FWHM of approximately 20 keV can be distinguished and its peak shape can also be found, as shown in Figure 6(d). However, it is impossible for the low-resolution FNAS to diagnose the accurate peak position, and the uncertainty could be up to 100 keV for the peak of 433 keV, as shown in Figure 6(e).

5. Discussion

FNAS is widely used in the field of neutron resonance[42], in which the neutrons are absorbed by the nuclei, forming a new compound nuclei, especially when the neutron energy close to the nuclei excited state energy has a large nuclear reaction cross-section. The compound nuclei are unstable, and they would release a neutron to decay to the ground state or by emitting γ photons (called radiation capture)[43]. By analyzing the cross-section data of the resonance energy region, we can obtain the parameters of the resonance energy levels, such as the energy, width (i.e., lifetime), spin and parity. However, for the higher energy neutron ($E_n > 100$ keV), a single resonance level can hardly be measured because the energy resolution of FNAS is not high enough or the compound nucleus energy levels overlap each other. In this situation, the average properties of the resonance energy levels are usually studied[4]: the average energy level spacing, strength function, etc. Now, due to the fact that the energy resolution of FNAS based on a laser plasma accelerator can be improved one order of magnitude higher than the state-of-the-art FNAS based on traditional accelerators, it can provide the possibility for studying more detailed nuclear structures and reaction mechanisms.

6. Conclusion

In conclusion, we have presented a method for realizing FNAS with an ultrahigh energy resolution based on a high repetition rate laser plasma electron accelerator. Firstly, we designed the electron accelerator by utilizing a 100-Hz terawatt laser system and a high-density nitrogen gas jet to drive the tightly focused laser wakefield acceleration, where the optimal electron beam has the maximum energy of approximately 25 MeV and the single-shot charge of approximately 2.5 nC. Secondly, we utilized the optimal electron beam to drive the photo-nuclear neutron source in a thin metal target, where the optimal neutron source has the yield of 7×10^5 neutrons/shot, the pulse duration

https://doi.org/10.1017/hpl.2023.92 Published online by Cambridge University Press

of approximately 50 ps, the energy range from 40 keV to 4 MeV and the peak energy of approximately 700 keV. Finally, we designed the ultrahigh energy-resolution FNAS, and displayed its potential in distinguishing the narrow fast neutron absorption peak. The FNAS based on the ultra-short pulse, high repetition rate fast neutron source has one order of magnitude higher energy resolution than the state-of-the-art FNAS, and is of great significance in promoting the study of more detailed nuclear structures.

Acknowledgements

This work was supported by the National Natural Science Foundation of China (Grant Nos. 11991073, 12305272, 12335016, 11721404, and 12074251), the Strategic Priority Research Program of the CAS (Grant No. XDA25030400) and the National Key R&D Program of China (Grant No. 2021YFA1601700).

References

1. A. S. Tremsin, S. C. Vogel, M. Mocko, M. A. M. Bourke, V. Yuan, R. O. Nelson, D. W. Brown, and W. B. Feller, Neutron News **24**, 28 (2013).
2. Y. Yu, R. Zhang, L. Lu, and Y. Yang, Appl. Sci. **11**, 6050 (2021).
3. M. Zimmer, S. Scheuren, A. Kleinschmidt, N. Mitura, A. Tebartz, G. Schaumann, T. Abel, T. Ebert, M. Hesse, Ş. Zähter, S. C. Vogel, O. Merle, R.-J. Ahlers, S. D. Pinto, M. Peschke, T. Kröll, V. Bagnoud, C. Rödel, and M. Roth, Nat. Commun. **13**, 1173 (2022).
4. D. J. Hughes, R. C. Garth, and J. S. Levin, Phys. Rev. **91**, 1423 (1953).
5. A. S. Tremsin, Neutron News **23**, 35 (2012).
6. I. D. Hau, T. R. Niedermayr, O. B. Drury, A. Burger, Z. Bell, and S. Friedrich, Nucl. Instrum. Methods Phys. Res. Sect. A **559**, 745 (2006).
7. V. W. Yuan, J. D. Bowman, D. J. Funk, G. L. Morgan, R. L. Rabie, C. E. Ragan, J. P. Quintana, and H. L. Stacy, Phys. Rev. Lett. **94**, 125504 (2005).
8. T. E. Mason, Phys. Today **59**, 44 (2006).
9. J. Wei, H. Chen, Y. Chen, Y. Chen, Y. Chi, C. Deng, H. Dong, L. Dong, S. Fang, J. Feng, S. Fu, L. He, W. He, Y. Heng, K. Huang, X. Jia, W. Kang, X. Kong, J. Li, T. Liang, G. Lin, Z. Liu, H. Ouyang, Q. Qin, H. Qu, C. Shi, H. Sun, J. Tang, J. Tao, C. Wang, F. Wang, D. Wang, Q. Wang, S. Wang, T. Wei, J. Xi, T. Xu, Z. Xu, W. Yin, X. Yin, J. Zhang, Z. Zhang, Z. Zhang, M. Zhou, and T. Zhu, Nucl. Instrum. Methods Phys. Res. A **600**, 10 (2009).
10. P. W. Lisowski and K. F. Schoenberg, Nucl. Instrum. Methods Phys. Res. Sect. A **562**, 910 (2006).
11. I. Pomerantz, E. McCary, A. R. Meadows, A. Arefiev, A. C. Bernstein, C. Chester, J. Cortez, M. E. Donovan, G. Dyer, E. W. Gaul, D. Hamilton, D. Kuk, A. C. Lestrade, C. Wang, T. Ditmire, and B. M. Hegelich, Phys. Rev. Lett. **113**, 184801 (2014).
12. Y. Li, J. Feng, W. Wang, J. Tan, X. Ge, F. Liu, W. Yan, G. Zhang, C. Fu, and L. Chen, High Power Laser Sci. Eng. **10**, e33 (2022).
13. J. Faure, Y. Glinec, A. Pukhov, S. Kiselev, S. Gordienko, E. Lefebvre, J.-P. Rousseau, F. Burgy, and V. Malka, Nature **431**, 541 (2004).
14. C. G. Geddes, C. S. Toth, J. Van Tilborg, E. Esarey, C. B. Schroeder, D. Bruhwiler, C. Nieter, J. Cary, and W. P. Leemans, Nature **431**, 538 (2004).
15. S. P. D. Mangles, C. D. Murphy, Z. Najmudin, A. G. R. Thomas, J. L. Collier, A. E. Dangor, E. J. Divall, P. S. Foster, J. G. Gallacher, C. J. Hooker, D. A. Jaroszynski, A. J. Langley, W. B. Mori, P. A. Norreys, F. S. Tsung, R. Viskup, B. R. Walton, and K. Krushelnick, Nature **431**, 535 (2004).
16. Y. F. Li, D. Z. Li, K. Huang, M. Z. Tao, M. H. Li, J. R. Zhao, Y. Ma, X. Guo, J. G. Wang, M. Chen, N. Hafz, J. Zhang, and L. M. Chen, Phys. Plasmas **24**, 023108 (2017).
17. J. Feng, Y. Li, J. Tan, W. Wang, Y. Li, X. Zhang, Y. Meng, X. Ge, F. Liu, W. Yan, C. Fu, L. Chen, and J. Zhang, Laser Photonics Rev. **17**, 2300514 (2023).
18. S. Kneip, C. McGuffey, J. L. Martins, S. F. Martins, C. Bellei, V. Chvykov, F. Dollar, R. Fonseca, C. Huntington, G. Kalintchenko, A. Maksimchuk, S. P. D. Mangles, T. Matsuoka, S. R. Nagel, C. A. J. Palmer, J. Schreiber, K. T. Phuoc, A. G. R. Thomas, V. Yanovsky, L. O. Silva, K. Krushelnick, and Z. Najmudin, Nat. Phys. **6**, 980 (2010).
19. A. J. Gonsalves, K. Nakamura, J. Daniels, C. Benedetti, C. Pieronek, T. C. H. de Raadt, S. Steinke, J. H. Bin, S. S. Bulanov, J. van Tilborg, C. G. R. Geddes, C. B. Schroeder, C. Tóth, E. Esarey, K. Swanson, L. Fan-Chiang, G. Bagdasarov, N. Bobrova, V. Gasilov, G. Korn, P. Sasorov, and W. P. Leemans, Phys. Rev. Lett. **122**, 084801 (2019).
20. B. Mahieu, N. Jourdain, K. T. Phuoc, F. Dorchies, J. P. Goddet, A. Lifschitz, P. Renaudin, and L. Lecherbourg, Nat. Commun. **9**, 3276 (2018).
21. W. Wang, K. Feng, L. Ke, C. Yu, Y. Xu, R. Qi, Y. Chen, Z. Qin, Z. Zhang, M. Fang, J. Q. Liu, K. Jiang, H. Wang, C. Wang, X. Yang, F. Wu, Y. Leng, J. S. Liu, R. Li, and Z. Xu, Nature **595**, 516 (2021).
22. L. T. Ke, K. Feng, W. T. Wang, Z. Y. Qin, C. H. Yu, Y. Wu, Y. Chen, R. Qi, Z. J. Zhang, Y. Xu, X. J. Yang, Y. X. Leng, J. S. Liu, R. X. Li, and Z. Z. Xu, Phys. Rev. Lett. **126**, 214801 (2021).
23. X. J. Jiao, J. M. Shaw, T. Wang, X. M. Wang, H. Tsai, P. Poth, I. Pomerantz, L. A. Labun, T. Toncian, M. C. Downer, and B. M. Hegelich, Matter Radiat. Extremes **2**, 296 (2017).
24. C. M. Brenner, S. R. Mirfayzi, D. R. Rusby, C. Armstrong, A. Alejo, L. A. Wilson, R. Clarke, H. Ahmed, N. M. H. Butler, and D. Haddock, Plasma Phys. Controll. Fusion **58**, 014039 (2016).
25. A. Yogo, S. R. Mirfayzi, Y. Arikawa, Y. Abe, T. Wei, T. Mori, Z. Lan, Y. Hoonoki, D. O. Golovin, and K. Koga, Appl. Phys. Express **14**, 106001 (2021).
26. K. Mima, A. Yogo, S. R. Mirfayzi, Z. Lan, Y. Arikawa, Y. Abe, and H. Nishimura, Appl. Opt. **61**, 2398 (2022).
27. I. Kishon, A. Kleinschmidt, V. A. Schanz, A. Tebartz, O. Noam, J. C. Fernandez, D. C. Gautier, R. P. Johnson, T. Shimada, G. A. Wurden, M. Roth, and I. Pomerantz, Nucl. Instrum. Methods Phys. Res. A **932**, 27 (2019).
28. D. Guénot, D. Gustas, A. Vernier, B. Beaurepaire, F. Böhle, M. Bocoum, M. Lozano, A. Jullien, R. Lopez-Martens, A. Lifschitz, and J. Faure, Nat. Photonics **11**, 293 (2017).
29. J. Faure, D. Gustas, D. Guénot, A. Vernier, F. Böhle, M. Ouillé, S. Haessler, R. Lopez-Martens, and A. Lifschitz, Plasma Phys. Controll. Fusion **61**, 014012 (2019).
30. F. Salehi, M. Le, L. Railing, M. Kolesik, and H. M. Milchberg, Phys. Rev. X **11**, 021055 (2021).
31. D. Papp, A. Necas, N. Hafz, T. Tajima, S. Gales, G. Mourou, G. Szabo, and C. Kamperidis, Photonics **9**, 826 (2022).

https://doi.org/10.1017/hpl.2023.92 Published online by Cambridge University Press

32. D. Gustas, D. Guénot, A. Vernier, S. Dutt, F. Böhle, R. Lopez-Martens, A. Lifschitz, and J. Faure, Phys. Rev. Accel. Beams **21**, 013401 (2018).
33. J. Feng, Y. Li, J. Wang, D. Li, C. Zhu, J. Tan, X. Geng, F. Liu, and L. Chen, High Power Laser Sci. Eng. **9**, e5 (2021).
34. T. D. Arber, K. Bennett, C. S. Brady, A. Lawrence-Douglas, M. G. Ramsay, N. J. Sircombe, P. Gillies, R. G. Evans, H. Schmitz, A. R. Bell, and C. P. Ridgers, Plasma Phys. Controll. Fusion **57**, 113001 (2015).
35. M. V. Ammosov, N. B. Delone, and V. P. Krainov, J. Exp. Theor. Phys. **64**, 1191 (1986).
36. E. Esarey, C. B. Schroeder, and W. P. Leemans, Rev. Mod. Phys. **81**, 1229 (2009).
37. S. Corde, K. T. Phuoc, G. Lambert, R. Fitour, V. Malka, A. Rousse, A. Beck, and E. Lefebvre, Rev. Mod. Phys. **85**, 1 (2013).
38. J. Feng, C. Fu, Y. Li, X. Zhang, J. Wang, D. Li, C. Zhu, J. Tan, M. Mirzaie, Z. Zhang, and L. Chen, High Energy Density Physics **36**, 100753 (2020).
39. W. Qi, X. Zhang, B. Zhang, S. He, F. Zhang, B. Cui, M. Yu, Z. Dai, X. Peng, and Y. Gu, Phys. Plasmas **26**, 043103 (2019).
40. J. Chen, L. Zhang, R.-Y. Zhu, Y. Du, S. Wang, S. Sun, and X. Li, IEEE Trans. Nucl. Sci. **65**, 2147 (2018).
41. https://www.nndc.bnl.gov/nudat3/nudat2.jsp.
42. M. Ooi, M. Teshigawara, T. Kai, M. Harada, F. Maekawa, M. Futakawa, E. Hashimoto, M. Segawa, M. Kureta, A. Tremsin, T. Kamiyama, and Y. Kiyanagi, Phys. Procedia **43**, 337 (2013).
43. X. Zhang, W. Wei, C. Fu, X. Yuan, H. An, Y. Deng, Y. Fang, J. Gao, X. Ge, B. Guo, C. He, P. Hu, N. Hua, W. Jiang, L. Li, M. Li, Y. Li, Y. Li, G. Liao, F. Liu, L. Liu, H. Wang, P. Yang, S. Yang, T. Yang, G. Zhang, Y. Zhang, B. Zhu, X. Xi, J. Zhu, Z. Sheng, and J. Zhang, Rev. Sci. Instrum. **89**, 023505 (2018).

https://doi.org/10.1017/hpl.2023.92 Published online by Cambridge University Press